metals

MDPI

Article

Numerical Modeling of Shockwaves Driven by High-Energy Particle Beam Radiation in Tungsten-Made Structures

Martina Scapin * and Lorenzo Peroni

DYNLab, Department of Mechanical and Aerospace Engineering,
Politecnico di Torino—Corso Duca degli Abruzzi, 24, 10129 Turin, Italy; lorenzo.peroni@polito.it
* Correspondence: martina.scapin@polito.it

Abstract: The investigation of wave propagation in solids requires the development of reliable methods for the prediction of such dynamic events in which the involved materials cover wide ranges of different possible states, governed by plasticity, equation of state, and failure. In the present study, the wave propagation in metals generated by the interaction of high-energy proton beams with solids was considered. In this condition, axisymmetric waves were generated, and, depending on the amount of the delivered energy, different regimes (elastic, plastic, or shock) can be reached. Nonlinear numerical analyses were performed to investigate the material response. The starting point was the energy map delivered into the component as the consequence of the beam impact. The evolution of both hydrodynamic and mechanical quantities was followed starting from the impact and the effects induced on the hit component were investigated. The results showed the portion of the component close to the beam experiences pressure and temperature increase during the deposition phase. The remaining part of the component is traversed by the generated shockwave, which induces high values of strain in a short time or even the failure of the component.

Keywords: high-energy impact; axisymmetric shockwave; finite element numerical simulation; Large Hadron Collider; refractory metals

Citation: Scapin, M.; Peroni, L. Numerical Modeling of Shockwaves Driven by High-Energy Particle Beam Radiation in Tungsten-Made Structures. *Metals* **2022**, *12*, 670. https://doi.org/10.3390/met12040670

Academic Editor: Denis Benasciutti

Received: 4 March 2022
Accepted: 11 April 2022
Published: 14 April 2022

1. Introduction

The understanding of the materials response in the case of high strain rate, impact, or shock loading conditions is fundamental in several applications, such as, e.g., ballistic, nuclear and military fields, and aeronautics and aerospace engineering. The involved materials can cover a wide range of different possible states and the processes to which they are subjected are significantly different from those related to quasistatic situations. This implies that the usual approaches for the evaluation of the mechanical response could be no longer valid.

In the present study, the interest was focused on the impact between high-energy particle beams and metals. The event is characterized by some peculiar features. The impact produces an energy transfer into the material, and the temperature increase could be significant and need to be considered. The time scale of the impact is typically shorter than the characteristic time of the mechanical response. The directly hit part of the component is subjected to a pressure increase that could be so high that it implies that the hydrodynamic response prevails on the mechanical one, resulting in a fluidlike behavior. Conversely, far regions of the component could remain in relatively low-pressure and low-temperature conditions, and the mechanical strength rules the dynamic material deformation. This preliminary overview allows to conclude that plasticity, equation of state (EOS), and failure are involved in the phenomenon, which is coupled from the thermostructural point of view.

The specific topic of the present paper deals with the numerical simulations using the finite element method of the shockwave propagation in matter due to radiation effects induced by high-energy proton beams in tungsten-made targets of the Large Hadron Collider (LHC) at CERN [1]. The construction and the design of such high-energy accelerators

brought the need of assessing the effects induced by potentially catastrophic events on the machine components in case of uncontrolled impacts. This aspect is further heightened by the study and the development of an increasingly energetic accelerator in the future (for example, the High Luminosity LHC upgrade [2], the Higher-Energy LHC [3], or the Future Circular Collider [4]). In recent decades, the researchers at several high-energy laboratories performed a great amount of studies to predict the response of specific components (such as beam intercepting devices, BID) properly designed for intercepting and absorbing particles or for shielding more delicate machine components in case of accidental events. Those studies had multiple objectives, which are summarized as follows: the investigation of the response of existing components, the validation of the use of specific materials, and the evaluation of new solutions, in terms of both design and materials, for next-generation components and machines.

A widespread approach for the comprehension of what happens in hit components in the case of high-energy particle beam impact is the numerical simulation, which needs two contributions. The first one is the evaluation of the thermal loads transferred into the materials by the interaction between high-energy particles and the atomic nuclei of the target [5–7]. It could be achieved thanks to the development of specific codes for particle transport simulations [8–14]. The amount and the distribution of the deposited energy mainly depends on the particle beam parameters (i.e., energy, intensity, and size) and on the target material itself (i.e., inelastic scattering length, radiation length, density, and atomic and mass numbers). For a fixed set of beam parameters, the higher the atomic number, the higher the peak of energy and the shorter its position in the target thickness (measured from the hit surface). The second contribution is the definition of numerical models to predict the mechanical evolution of the phenomenon and the effects induced on the hit structures. By considering the scientific literature, several studies were performed by changing the beam parameters (size, intensity, and number of bunches), the impact scenario (type of beam and position of the impact), the hit targets (shape, geometry, and functionality), the hit materials (copper and copper composites, tungsten and tungsten alloys, iridium, carbon and carbon-based materials, etc.), and the codes used for calculations (BIG2 [15], Ansys Autodyn [16], LS-DYNA [17] were the most widely used). In the numerical solutions, several approaches were followed, generally divided in pure hydrodynamic or thermostructural calculations. In the following, a bibliographic review is reported with the aim to highlight the main differences in the applied methodologies of simulation. The interest was limited to the studies in which the targets were made in a metallic material. In case of pure hydrodynamic models, as performed in [18–22], the target was considered like a fluid, hence the thermal loads effects were investigated only on pressure, density, and temperature and the definition of a multiphase equation of state (EOS) was sufficient to solve the problem. In [23], thermostructural calculations were presented: the loading condition imposed to the hit target was the thermal load obtained from the deposited energy and calculated by considering a linear EOS. A similar approach was used also in [24,25] in which under the hypothesis that no changes of state occurred, numerical analysis were performed for the simulation of oscillations induced in the target. In [26,27], strength and failure models were combined with the Mie–Grüneisen EOS suitable in case of not too high pressure. In [28–32], more sophisticated models were defined: multiphase EOS were used to convert the deposited energy in temperature and pressure increase and to evaluate the hydrodynamic behavior (in terms of pressure, density, and temperature/energy evolutions) while the deviatoric component of stress was described by defining specific elastoplastic constitutive models and, in some cases, also failure models. More advanced simulations were proposed in [33–38], in which, by following different approaches and methodologies, the map of the energy deposition was updated considering the evaluated change in density due to the shockwave propagation in case of multiple impacts on the same target. All of the previously cited studies were performed with implicit or explicit integration schemes in case of a Lagrangian solution. In [39], a smoothed-particle hydrodynamics (SPH) technique was adopted to simulate the particle projection.

Shock and impact techniques provide an important source of data to investigate the hydrodynamic behavior of matter, especially in extreme conditions that cannot be investigated using other methods. Another important reason to use this type of experiments is to investigate material changes, which could occur during the shockwave passage. In this sense, it is possible to investigate physical, chemical, and metallurgical changes, phase transition, fragmentation, etc. With these aims, in the last ten years, in addition to what could be obtained as results from numerical simulations, a significant improvement in the comprehension of the high-energy beams/matter interaction came from experimental tests performed in the facility, called High Radiation to Materials (HiRadMat), developed at CERN [40]. It is a dedicated facility specifically designed to impact in a safe and controlled manner materials and accelerator components with intense and energetic proton or ion beams. Limiting the attention to experiments related to targets and BID components, several experiments were performed starting from 2012 on materials [41–43] and components [44–46]. Generally speaking, the main objectives were to validate the results obtained from the numerical simulations and to collect data on the materials response in such extreme loading conditions, especially for nonconventional and novel ones. The experiments were preceded by intensive research activities aimed to identify the case studies and the loading conditions. Other important aspects concerned the evaluation of which quantities and properties it was possible or necessary to measure and which are the most suitable measuring systems to catch the evolution of the phenomena. The postprocessing phases of many of those experiments are still in progress, in continuous development, and under evaluation to setup new experiments [27,47–49].

The present study proposes a methodology for the prediction of the mechanical behavior of metal structures subjected to high-energy impact. The methodology is specifically applied to simulate with the nonlinear FE code LS-DYNA the shock generation and propagation induced in a tungsten-made structure by the accidental beam loss of some bunches of an LHC collimated proton beam. This particular case was chosen as a case study because it allows us to highlight the criticalities of such events, especially because the energy absorbed is high for tungsten. The proposed methodology was tuned thanks to the experience gained from the critical review of the different numerical procedures proposed for the simulations of the materials/components behavior in case of high-energy particle beam impact. After a decade of numerical research studies on this topic, the present work takes advantages from the analysis of the main assumptions and hypothesis applied to such a particular and exotic class of shockwave phenomena in order to overcome the limitations encountered in previous research studies. In addition, the methodology applied for the analysis of results allows us to clearly investigate any aspects of wave propagation.

2. High-Energy Particle Beam Impact

When high-energy particles pass through solid matter, they lose energy, which is transferred to the material lattice, increasing its temperature and pressure in a few nanoseconds. The energy transfer could be considered isochoric because the change in pressure and temperature is faster than the mechanical response of the lattice (the material is not able to expand). The event provokes a dynamic response of the structure inducing thermal stress waves, thermal vibrations and the generation of waves, but depending on the several parameters, different situations can be expected. Among the big number of influencing parameters, the most important are the distribution of the deposited energy, the energy density, the timescale of the phenomenon, the material properties, and the impact scenario. In the following, each of them is examined.

Typically, in the particle accelerators, the beam is not continuous, but is it made of a series of particle bunches, each spaced by a time interval. A possible configuration is reported in Figure 1 in which each bunch duration is 0.5 ns and the time interval between two successive bunches is 25 ns.

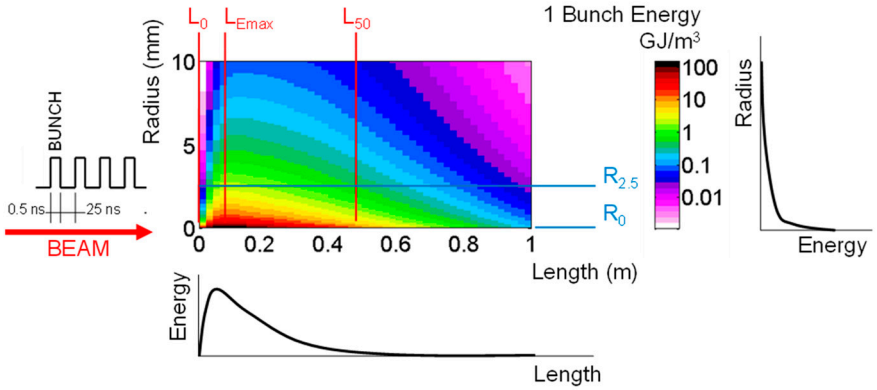

Figure 1. Distribution of the deposited specific energy (GJ/m^3, logarithmic scale) in a tungsten block hit at the center of one basis (result of the FLUKA calculation [33]).

The spatial distribution of the deposited energy inside the material is influenced by the size and the parameters of the beam and by the energy absorption capability of the material. As mentioned in the Introduction, the evaluation of the thermal load produced by the particle/matter interaction needs to be performed by specific codes for particle transport simulations [8–14]. They must take into account that when a high-energy particle beam interacts with a target, the particles first interact with the electrons of the lattice of the impacted material and successively with the nuclei, producing a cascade (shower) of secondary particles. This calculation is out of the scope of the present study, but it represents the input data for the mechanical analysis of the effects induced by the impact starting from the map of the absorbed energy. In Figure 1, there is an example of the specific energy deposited in a block hit at the center of one basis. Independently from the impact condition, it is convenient to define a reference system identified by the axis of the beam (longitudinal direction) and the distance from the axis of the beam (radial direction). The distribution of the deposited energy varies both longitudinally (i.e., in the beam direction) and in the transversal plane with respect to the beam direction and can be sampled by a Gaussian distribution. The map of the energy distribution can be also displayed as a function of the length for a fixed radius or as a function of the radius for a fixed length. In the scheme of Figure 1, three longitudinal coordinates are highlighted, which will be useful for the analysis of the results described in the following: L_0 identifies the impacted base of the component, L_{Emax} identifies the depth in which there is the maximum of the absorbed energy, and L_{50} is the half of the component. Similarly, in the radial direction, R_0 is the beam axis and $R_{2.5}$ is the situation at a distance of 2.5 mm from the beam axis. From the diagram of the energy by varying the length, it is possible to notice that the maximum of the deposited energy is at a certain depth from the hit surface; this mainly depends on the material, indicating its stopping power capability. The density strongly influences the deposited energy: higher values of energy are expected for denser materials, for which the peak is situated at the smallest distance from the impacted face. In addition, the density is strictly correlated with the prediction and the evaluation of the tunneling effect [33]: a variation of the density along the beam axis (such that could occur as a consequence of the shockwave propagation) modifies the material properties, reducing the effectiveness of its shielding to successive bunches and requiring a new calculation of the deposited energy based on the effective density distribution. The energy distribution as a function of the radius (at each depth of penetration) indicates how local or widespread the energy distribution is and how sharp or smooth the transitions are, depending on the standard deviation, which physically expresses the deviation of the particles from the ideal trajectory (i.e., the beam axis) and therefore is often used to define the beam transverse size.

Depending on the amount of energy, different situations can develop. When the deposited energy is low, the dynamic response remains in the elastic regime, in which the vibrations and stress waves are low enough to not exceed the elastic limit of the material, which is able to completely recover the induced deformation. In this condition,

the changes in density are negligible and the stress waves travel in the material at the speed of sound. By increasing the amount of energy, the materials enter the plastic domain with permanent deformation induced. In case of uniaxial stress, because the slope of the stress–strain relationship is lower in the plastic domain than in the elastic one, the propagating velocity of the plastic wave is lower. This is because at a fixed strain, it is proportional to the square root of the slope of the flow stress curve. As a consequence, there is the dispersion of the wave due to the decrease of the wave velocity with increasing stress. Considering the opposite situation characterized by a uniaxial strain state, the stress–strain relationship must also include the EOS. In the case of nonlinear stiffening EOS, the stress–strain relationship beyond the elastic limit becomes concave. This implies that there is a point on the stress–strain curve beyond which the plastic waves start to be faster than the elastic precursor. Beyond this limit, the wave velocity continues to increase with plastic strain leading the plastic wave front to steepen up and then propagate as a shock front. This is what happen when a high level of energy is deposited: shockwaves are generated, and the mass transport phenomenon could become relevant. In addition to the previous consideration, in the part of the component in which the energy is high, the bulk material response is much more similar to that is expected for a fluid. However, the pure hydrodynamic treatment of the shock propagation is overly simplified and fails to correctly predict the complexity of the involved phenomena [50].

Another aspect to be considered is the ratio between the lateral dimensions of the hit structure and the spatial distribution of the absorbed energy in the lateral (radial) direction. If the particle beam impacts a thin rod, the problem is ideally one-dimensional, and for the component, a uniaxial stress state could be considered. Conversely, when the particle beam impacts a wide structure, axisymmetric waves are generated.

The duration of the energy deposition strongly influences the evolution of the phenomenon. Mainly, two different situations can arise depending on the ratio between the energy release timescale and the characteristic time of the system. One case is when the deposition time is shorter than the heat diffusion and the mechanical response times. For example, this happens in the case of accidental beam loss in particle accelerators; for these events, the time scale typically is in the order of magnitude of nanoseconds or microseconds. In this situation, from the mechanical standpoint, the deposition is quasi-instantaneous, and the pressure and energy increases occur at constant density (i.e., isochoric heating). Conversely, in the case of long-term energy deposition, the time scale is higher and the system has time to react before the end of the deposition itself.

The possible impact scenarios are summarized in Figure 2. If the impact occurs inside the material (i.e., not close to free surfaces, point A and B), the traveling of the generated wave propagation produces the compression of the material above the wave front and the rarefaction of the material behind it. When the wave reaches the free surfaces, it is reflected back as a tensile wave, and depending on its residual level of stress (after the attenuation due to the propagation), it could be able to provoke the spallation fracture (with fragment projection) or to produce the deformation (plastic or elastic bulge) of the free surface. The last two possibilities are the same which could develop if relatively low energy impact occur near the free surface. Otherwise, in the case of high-energy impact near the free surface (point C), the change of state could involve the material up to the free surface; in this condition, the reflected wave could not be supported by the material and the effect is the spray of liquid, gas, or solid parts.

The previous considerations exemplify the complexity of the problem, which needs a multiphysics approach to be completely examined. As a matter of fact, different subjects are involved, such as physics, thermodynamics, engineering, and materials science. In order to correctly get the thermomechanical response of the impacted material from FE numerical simulations, it is necessary to take both the hydrodynamic behavior, adopting a dedicated equation of state (EOS), and the deviatoric behavior, resorting to dedicated strength and failure material models, into account.

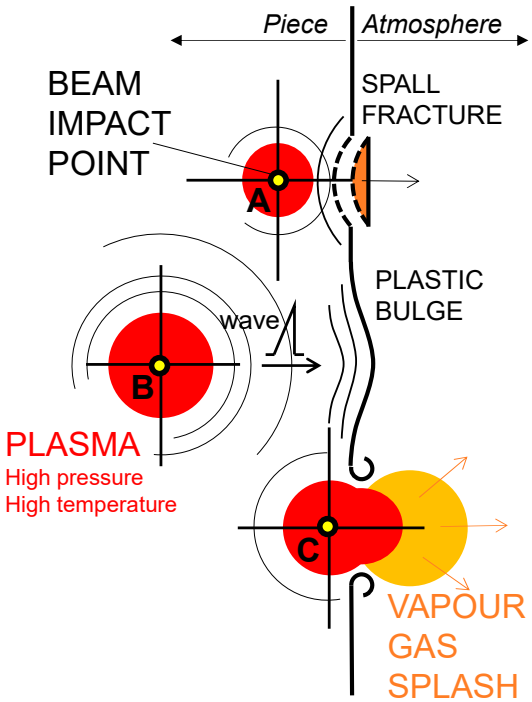

Figure 2. Scheme of the possible scenarios in case of particle beam impact against a solid target: the cases A and B represent an impact occurring far from a free surface; the case C indicates an impact occurring close to a free surface.

3. Research Method and Procedure

The high-energy particle beam impact scenarios involve extreme conditions mainly characterized by high pressure, high temperature, and high rate of deformation. As anticipaed in the previous section, the direct effect of the particle beam impact is to induce a jump in pressure and temperature, which could also directly produce the change of state where the deposited energy is high. The impact also generates waves that travel inside the material, leading also the rest of the component, placed far from the high-energy zone, to reach high values of strain and temperature in a short time (i.e., high strain rate).

The prediction of these phenomena needs to be treated with the use of finite element numerical simulations performed with an explicit nonlinear code. The spatial variability requires the discretization of the domain, and among the several possibilities, the FE method is the most suitable and sensible. A specific value of energy must be deposited inside each element with a time profile able to replicate the real bunch profile of the particle beam. Usually, 3D solid elements should be used, but depending on the specific case, the computational time can be reduced by using 2D solid elements (e.g., plain strain or axisymmetric formulations). In this type of problem, the nonlinearities are mainly due to the material law for plasticity and damage, the multiphase EOS, and the high levels of deformation. Them within the time scale of the involved phenomena justify the adoption of the explicit integration scheme. All of the mentioned requirements suggest that LS-DYNA code is suitable for the solution; it has a general purpose transient dynamic explicit solver with nonlinear thermomechanical capabilities.

Before discussion of the simulation of the high-energy particle beam impact against a solid structure, it is necessary to recall some fundamentals of shock.

Planar and Cylindrical Waves

Usually, the shock propagation is investigated with reference to planar impact for different scenarios: hypervelocity impacts, shock tubes, and explosions. In general, at least in the portion of material in which the shock is generated, a uniaxial strain state is generated, while the stress state is three-dimensional. A complete and exhaustive treatment

of the shockwave propagation in solids and high-velocity impact dynamic phenomena can be found in [50–52]. The complete treatment of the shock theory is out of scope for the present paper; in this section, the main features of a shock are reported with the aim to identify and collect the necessary tools to cope with the comprehension of the results obtained from numerical simulations in case of high-energy particle beam impacts.

In general, a shock is characterized by a propagating surface in which the displacement is continuous, but other properties, such as density, pressure (or stress), particle velocity, and in general, the other thermodynamic quantities are discontinuous. In Figure 3, a simplified configuration of the typical pressure profile obtained in case of plate impact of a finite duration is reported as a function of both time and spatial coordinate (corresponding to the shock travel direction). The pressure shock wave consists of a shock front, a flat top with a finite time/spatial duration, and a release tail (release wave), which is the portion of the shockwave coming after the peak of pressure. This wave profile is typically obtained in case of the impact of a projectile. Otherwise, when the shock is produced by an explosive or a laser pulse, the shape of the shockwave is triangular [53].

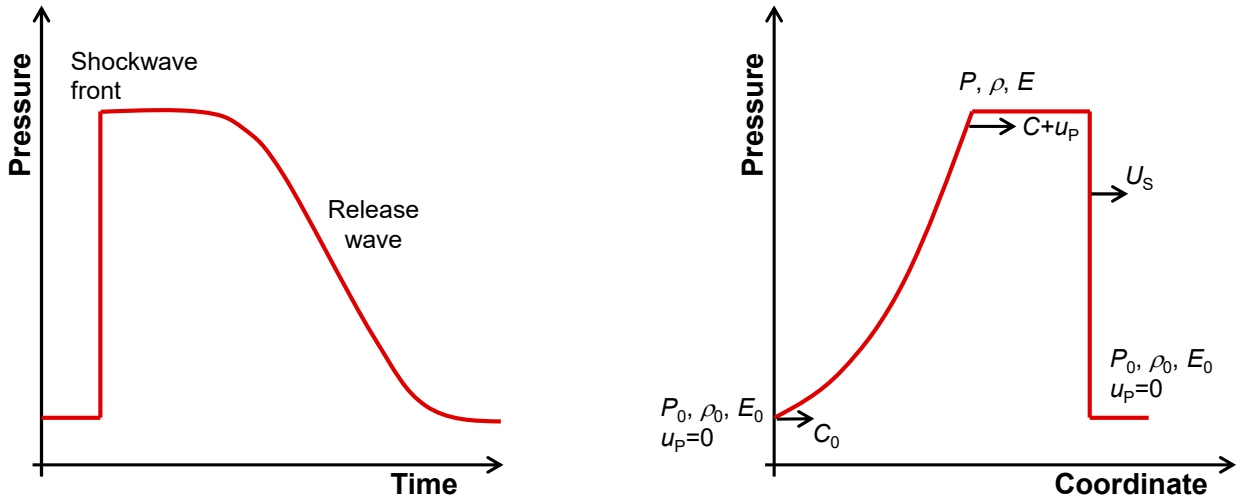

Figure 3. Pressure profile in case of plate impact: in function of time (**left**) and spatial coordinate (**right**). P, ρ, E, C, and U_p identify respectively pressure, density, energy, speed of sound, and particle velocity of a point belonging to the shocked material; P_0, ρ_0, E_0, C_0, and U_{p0} identify pressure, density, energy, speed of sound, and particle velocity in the undisturbed material, respectively; U_s is the shock front velocity with $C + U_p > U_s$.

Generally, the plastic wave front is preceded by the elastic precursor, but when the pressure level is high, the shock front overtakes it; no signals move ahead of the shock front, which is traveling at velocity U_S, being supersonic relatively to the undisturbed material, in which the sound of speed is c_0. Another important consideration to take in mind is that beyond the elastic regime, the sound speed continues to increase with pressure, if a stiffening EOS is considered because the pressure grows faster than linearly with the volume. In addition, when a wave travels in a shocked material, the fact that particles are moving at velocity u_P has also to be considered. Then, two considerations can be derived. The first is that a disturbance front, which can be also quite smooth at the beginning, continues to steepen up (becoming a shock front) while traveling into the material (as schematically represented in Figure 4); this is because the higher amplitude parts of the front travel faster than the lower amplitude ones. The second consideration regards the release wave. It travels in the shocked material (in which the particles are moving at velocity u_P). Hence, by traveling, the release wave reduces the duration of the shock, and there could be a time in which the top of the release wave reaches the shock front reducing it intensity (and as a consequence also its speed). This also means that any disturbance can catch the shock front from behind (the shock front is subsonic relative to

the shocked material). This is particularly evident in case of extremely short waves, such as those generated with laser energy deposition [53].

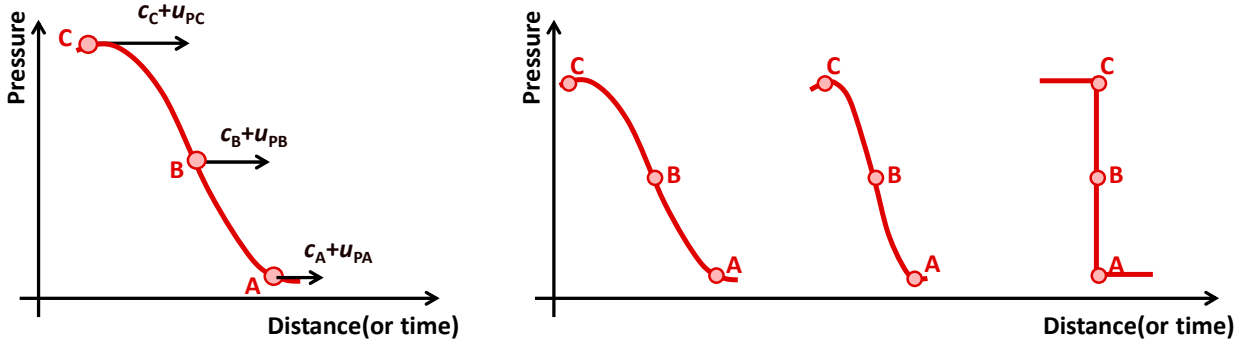

Figure 4. Explanation of the formation of a shock front starting from a smooth wave beyond the elastic limit; at each point, the velocity of the pressure wave is the sum of the speed of sound and the particle velocity proper of the conditions in which the point is ($C_C + U_{pC} > C_B + U_{pB} > C_A + U_{pA}$).

The high energy deposition inside the material produces a loading condition for which the cylindrical assumption is more realistic. At the beginning of these phenomena, the spatial pressure distribution is strictly related to the energy distribution deposited in the material (Figure 1). During the subsequent phase of propagation, the shockwaves generated in the material maintain an axisymmetric shape. This introduces some peculiarities that differentiate the wave propagation from those expected for the planar case (Figure 3). The scope of the present study is to analyze the results obtained from the numerical simulations of the high-energy impact with reference to what is expected from the wave propagation for cylindrical waves and underlying the differences with the more common mechanical impact scenarios. The rigorous mathematical solutions of the partial differential equations governing the propagation of planar and cylindrical waves are not presented here for sake of brevity, but they can be found in [54]. Since the numerical approach is the basis of the present study, it was also applied for this preliminary investigation. To this end, two simple numerical models were built for the visualization of the differences between planar and cylindrical shocks (Figure 5). The finite element simulations were performed with the software LS-DYNA. For the planar case, the geometry was modeled with shell elements in plain strain formulation and the uniaxial strain condition was obtained by fixing the nodes to not move in the y direction; in this way, the lateral deformation was prevented. In the cylindrical model, the geometry was modeled with shell elements with an axisymmetric formulation and the axial displacement were constrained; hence, only the radial displacement is allowed. In this second model, the component is an expanding ring. In each model, a rectangular velocity profile was imposed to a row of nodes; the velocity was in the x direction with a duration of about 2 μs and a maximum value of 300 m/s. The component is supposed to be in tungsten (density ρ_0 = 19255 kg/m^3) and the material behavior was modeled with a pure hydrodynamic material model whose behavior was completely defined by a linear EOS (bulk modulus B = 417 GPa).

In the case of a planar (or longitudinal) wave, the variables (e.g., pressure, particle velocity, density, etc.) depend on only one coordinate (e.g., the longitudinal one, called x) and on time. As a consequence, at a fixed time, the variables are homogeneous on a plane orthogonal to the direction defined by that coordinate. The direction of propagation is parallel to the longitudinal coordinate and the wave front is a plane normal to this direction (each section of material is moved in the propagation direction parallel to the other ones). The amplitude of the wave remains constant during the propagation, at least until the release wave will catch the front and after the passage of the release wave, the material returns to the undisturbed condition. These features were confirmed by the analysis of the numerical results. From the numerical point of view, the wave propagation was visualized by considering the pressure as a function of the longitudinal coordinate at different times

(Figure 6a); farther portions are invested by the pressure wave at a later time. The curves at increasing time show that the wave front was becoming sharper while the slope of the release wave was decreasing, implying a reduction of the duration of the shock and potentially being able to reduce the shock amplitude (and as a consequence, also the shock front velocity) if it catches the front (this is not the case shown in Figure 6a).

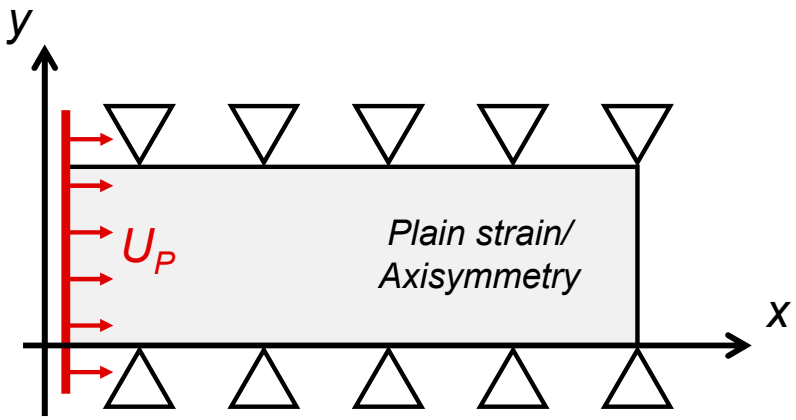

Figure 5. Scheme of the numerical models used for the investigation of the propagation of planar and cylindrical waves in solids: formulations, boundary conditions, and constraints.

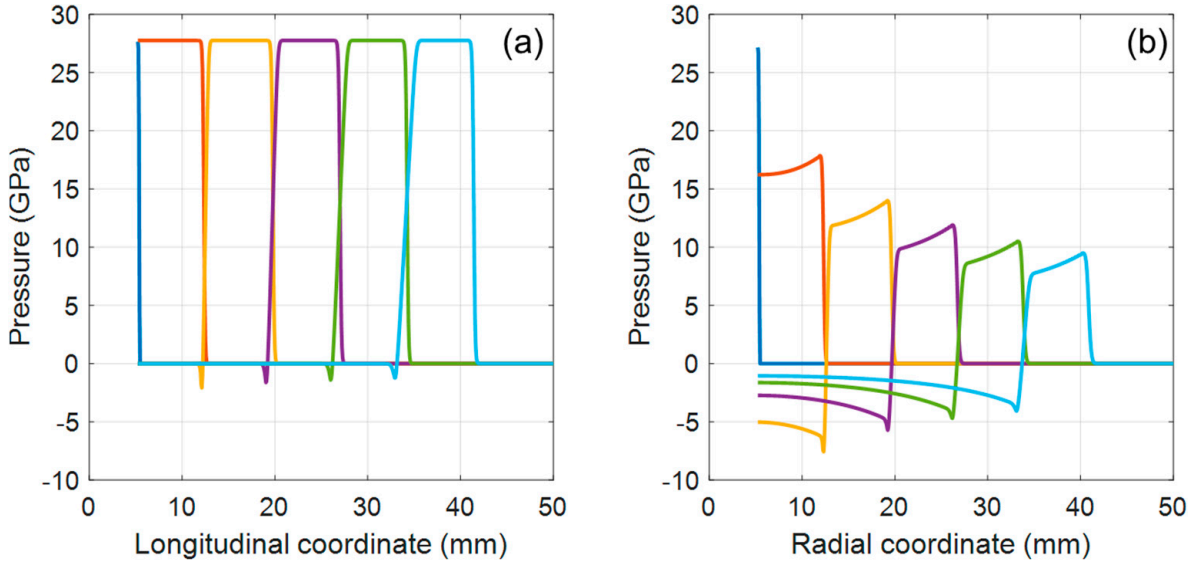

Figure 6. Pressure as a function of longitudinal coordinate for plane strain case (**a**) and pressure as a function of radial coordinate for the axisymmetric case (**b**) at different times.

Conversely, when a cylindrical coordinate system is considered and under the assumption of cylindrical symmetry, the variables depend on only the radial coordinate r and time. The solution of the wave equation, at a sufficiently large distance from the axis of the cylinder, gives that the amplitude of the shock decreases with the radius and, in particular, the decrement is proportional to $r^{-1/2}$ and the intensity of the wave decreases with $1/r$. Intuitively, this can be understood by thinking that when the cylindrical wave moves toward increasing radii, the same energy amount is distributed over a cylindrical surface whose area increase linearly with the radius. Another important difference between planar and cylindrical cases is that in the case of cylindrical waves, behind the shock front, there is always a negative pressure state (positive hydrostatic stress) that comes from the axisymmetric constraint itself. The fact that the material does not return in the

undisturbed condition implies that not only the pressure is not zero after the shock end, but also that particle velocity and density do not return to their initial values. When the shock amplitude is moderate, the change in density remains limited: the material is still solid and can support tensile load. When the shock is strong, the consequent change in density can be significant and the material could undergo a change of state, being unable to support hydrostatic tensile load (the material is no longer solid). These considerations were confirmed by the numerical results. For the cylindrical case, the wave propagation investigated by considering the pressure as a function of the radial coordinate at different times (Figure 6b). By focusing the attention on a point of the pressure wave (e.g., the peak of pressure of the shock front), it is possible to clearly observe the reduction of the amplitude while the wave is traveling. In addition, another important consideration is that with an imposed flat boundary condition in velocity, because of the axisymmetry, it is not possible to obtain a flat pressure profile, but the pressure decreases during the shock phase itself. At the end of the shock, the pressure reached negative values in the entire portion of material behind the end of the shock. If no limits are imposed, the material can reach high values of negative pressure (depending on the pressure level reached at the end of the shock). Otherwise, a limit can be defined in the FE model corresponding to the maximum hydrostatic tensile stress which can be supported by the material (this is not the case shown in Figure 6b). In particular, the negative pressure can be limited by imposing that a pressure lower than a threshold P_{min} (with $P_{min} < 0$) is not allowed (e.g., to simulate the material change of state and/or its loss of capability to support higher negative pressure).

4. Tungsten Component Impacted by LHC Proton Beam

As case study, a cylindrical bar made in tungsten was considered as the target. It was hit at the center of one base by eight bunches of the LHC at 7 TeV (standard deviation of the beam equal to 0.88 mm and 1.15×10^{11} protons per bunch; for more details, see [33]). The bunch length was 0.5 ns and the time between two successive bunches was 25 ns: the total duration of the deposition phase was about 200 ns. The simulated case is a possible accidental event for the LHC collimation system, and the duration of the deposition could correspond to the time before the protection system of the LHC starts to dump the beam. In nominal operating conditions, the collimators, which are placed close to the beam, intercept and stop particles of the external halo. In accidental scenarios, when the beam is out of control, collimators, which are strategically positioned, absorb the particle impact, thus protecting other critical structures, such as the superconducting magnets. The LHC collimation system is made up of several collimators placed along the LHC ring. The study of the possible damage of the collimators is a crucial issue due to the fact that they are the closest components to the proton beam.

The evaluation of thermal loads was performed by the FLUKA Team at CERN, using the FLUKA particle physics MonteCarlo simulation package [8,9]. Then, the FLUKA results obtained in GeV/cm^3/proton were converted to J/m^3 and used as input for the finite element analysis. The hypothesis of isolated bunches was made, which means that the reactions generated by the first bunch were assumed to be finished before the arrival of the second bunch and so on. Another assumption made in the present study was to neglect the tunneling effect. Theoretically, the FLUKA results are correct only for the first bunch that is impacting against a pristine material. The successive bunches encounter a material in which shockwaves were generated and propagated inducing modifications in some materials properties, such as the density. The results obtained in [33] demonstrated that in the case of the impact of a limited number of bunches, the induced modifications are not significant to require the update of the FLUKA calculation.

The FE numerical simulation was performed using the nonlinear code LS-DYNA [17] with a Lagrangian approach and an explicit integration time scheme. A multiphase EOS from the SESAME library was used combined with the definition of strength and failure models. The detailed description of the numerical model and the analysis of the results are reported in the following sections.

Description of the Numerical Model

The geometry considered was a cylinder 1 m long and with a radius of 10 mm impacted perpendicularly at the center of one base. The numerical model represented the irradiated parts of a bigger component. This means that the external surface was not modeled as a free surface, so there were not any reflections at the boundary, simulating, in this way, the presence of other material. The geometry of the target and the thermal load were axisymmetric, and this allowed to reduce the 3D problem to a 2D one [55].

The time step of the explicit analysis was set equal to about 0.1 ns in order to correctly appreciate the bunch profile (0.5 ns). The FE analyses were performed using underintegrated (1 integration point) 2D axisymmetric elements. The model counted 50 elements in the length (i.e., axial) direction and 100 elements in the radial direction: the elements dimension was 20 mm × 0.1 mm. The study of the mesh influence for a similar case was performed in [56] and showed that these values are a good compromise between solution accuracy and computational costs. The FLUKA calculation was also performed on the same 2D axisymmetric geometry with the same spatial discretization (bin size equal to element size). The FLUKA results converted in GJ/m^3 are shown in Figure 1 where a logarithmic scale was used for the visualization. The energy as a function of the radius at various axial coordinates and the energy as a function of the length at various radial coordinates are shown in Figure 7. The peak of the energy was about 150 GJ/m^3 and occurred along the axis of symmetry (r = 0 mm, R_0) at a depth of 60 mm from the impacted base (L_{Emax}).

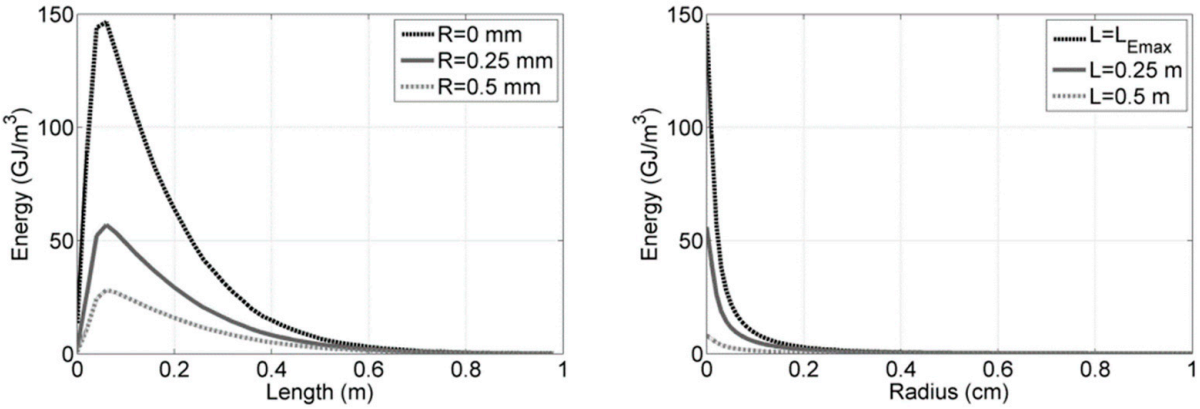

Figure 7. Distribution of the specific energy deposited from a single bunch on tungsten cylindrical bar (result of the FLUKA calculation): energy as a function of the axial direction curves varying the radial coordinate (**left**) and energy as a function of the radial coordinate varying the axial coordinates (**right**).

The plastic flow stress was described by the Johnson–Cook (J–C) formulation [57] including strain, strain rate, and temperature effects on based on the relationship $\sigma = (A + B\varepsilon^n)(1 + C\log\frac{\dot{\varepsilon}}{\dot{\varepsilon}_0})\left(1 - \frac{T - T_{room}}{T_{melt} - T_{room}}\right)$, for which the parameters are listed in Table 1. The failure of the component was simulated by an element erosion criterion that limited the negative pressure at low density. This criterion was introduced to simulate that where the component is no longer solid (e.g. a change of state occurred), the material is not able to support negative pressure (tensile stress); on the basis of the expected behavior in the case of a cylindrical shockwave, as described before, this could happen in the portion of material behind the shock front. From the point of view of the stability of the numerical solution, the erosion criterion also avoided too high distortion of the numerical mesh in a portion of the component with a negligible strength. At each time step and for each element, the FE solver performed the check of the erosion condition; if at the same time, both the pressure and the density became lower than the corresponding imposed limits, the element was deleted from the model. In detail, the threshold in pressure was set equal to zero and that in density was set equal to 14,600 kg/m^3. In addition, a limit for the

hydrostatic negative pressure (P_{spall}) was also defined to take spallation of the material into account [58]; if the computed pressure became lower than P_{spall}, the element was excluded from the calculation.

Table 1. J–C parameters for tungsten [59].

Parameter	Value	Unit	Parameter	Value	Unit
ρ_0	19,255	kg/m^3	$\dot{\varepsilon}_0$	1×10^{-3}	s^{-1}
G	1.6×10^{11}	Pa	m	0.41	-
ν	0.33	-	T_{melt}	3683	K
A	3.30×10^8	Pa	T_{room}	300	K
B	1.03×10^9	Pa	c_p	135.68	J/(kg K)
n	0.02	-	P_{spall}	-1.2×10^9	Pa
C	0.03	-			

The EOS used for the prediction of the hydrodynamic component of stress was the polynomial formulation defined in LS-DYNA [17]. The coefficients were obtained fitting the multiphase tabular EOS number 3550 of the SESAME library [60]. The procedure for the identification of the coefficients was automatically performed for each element at fixed times, considering a limited portion of the entire table. At a specific time and for each element, the considered portion on the EOS surface was centered in the point defined by pressure, density, and energy proper of that element. This meant that a specific EOS was defined for each element, and it was updated when the element condition in terms of computed pressure, density, and energy fell outside the range used for the previous polynomial interpolation. The EOSs were also used to introduce the specific energy obtained from FLUKA inside each element. This was performed defining a temporal load curve following the bunches profile. The numerical simulation ended at 1 µs, in order to simulate the propagation phase in free conditions (after 200 ns, there were not any new bunches impacting the structure).

5. Results and Discussion

The numerical results are shown in terms of pressure, density, temperature, and particle velocity in Figures 8–12, where the time/spatial distributions of those quantities are reported at different locations according to the definition of Figure 1. The maps show the time evolution along a coordinate (along the radius at a fixed length or along the length at a fixed radius). This is a typical representation of 1D wave propagation used in this case in order to highlight and better understand the evolution of radial and axial waves. The temperature scale was limited to the melting value at nominal density (3683 K; see Table 1). The white area represents the part of the component deleted from the calculation if one of the following criteria are satisfied; the erosion condition (negative pressure and low density), the spalling criteria (see Table 1) and negative pressure computed on elements in which the temperature exceeds the T_{melt} (see Table 1). This allows a rough estimation of the damage in the component.

Figure 8 shows the results as a function of time and radius for the axial coordinate corresponding to the peak of the deposited energy, called L_{Emax} (i.e., 6 cm from the impacted base). The maps show that the radial wave started immediately after the deposition of the first bunch. In the part of the component in which the deposited energy was high, the pressure remained approximately constant during the deposition phase; the increase in pressure due to the arrival of a new bunch compensated the pressure reduction due to the expansion during the time interval between two bunches. This created a roughly stationary pressure wave with a time duration equal to the deposition phase. The shape of the shockwave changed during the traveling because the release wave overtook the front. As a matter of fact, the speed of the release wave was higher than the speed of the shock front because it was moving in a compressed medium. This reduced both the level and the time duration of the wave, which became shorter and narrow (as also in shockwaves

produced with nanosecond duration lasers [53]). As mentioned in the previous section, this is not the unique reason for the reduction in the intensity of the shock, which was also reduced for geometric reasons, as the energy was spread over an increasing volume. The energy deposited by the first bunch was sufficient to overcome the T_{melt} in a cylinder of 1 mm of radius; the molten part became a cylinder of 3 mm of radius at the end of the deposition. This means that during the deposition phase, the wave front was moving inside molten material. At about 600 ns, the wave front reached a radius of 3 mm investing solid material. Far enough away from the beam axis, the deposition induced a continuous increment in pressure and temperature but with much lower values with respect those of the central part. In this portion, which was still solid at the end of the deposition, the strong modification of the state was induced when the front arrived; a significant increment of both pressure and energy was induced by the front while the change of phase occurred because of the arrival of the release wave. The part of the component behind the wave front was characterized by a reduction in density. Conversely, the density increased when there was the passage of the shock front: when the shockwave, even if attenuated, hit the almost pristine (at least in density) material, it was able to induce high compression states. The map of the particle velocity in the radial direction shows as the material flowed from the center to the external at velocity higher than 1 km/s projecting the internal plasma toward higher radii.

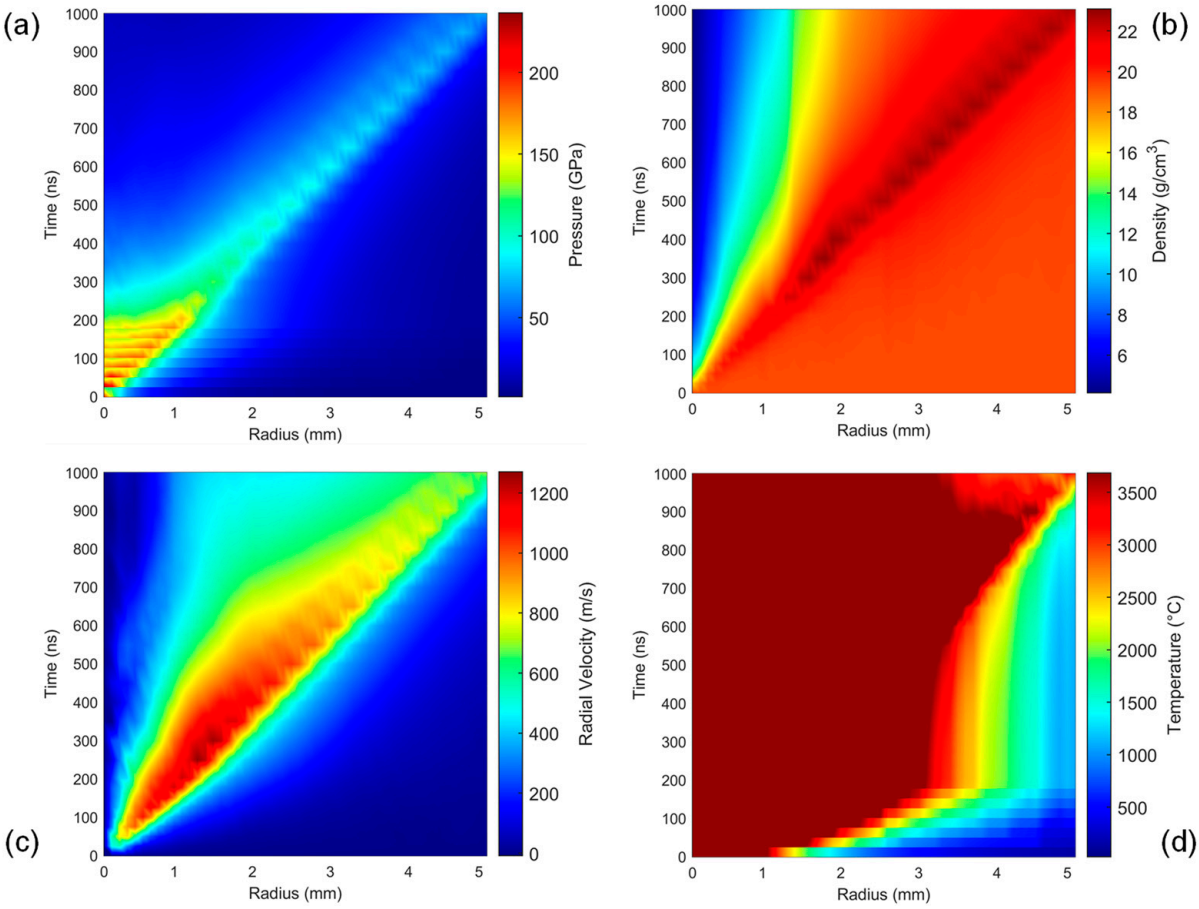

Figure 8. Pressure (**a**), density (**b**), particle velocity in radial direction (**c**), and temperature (**d**) distributions by varying the radius at the axial position of the maximum energy deposition (L_{Emax} of Figure 5).

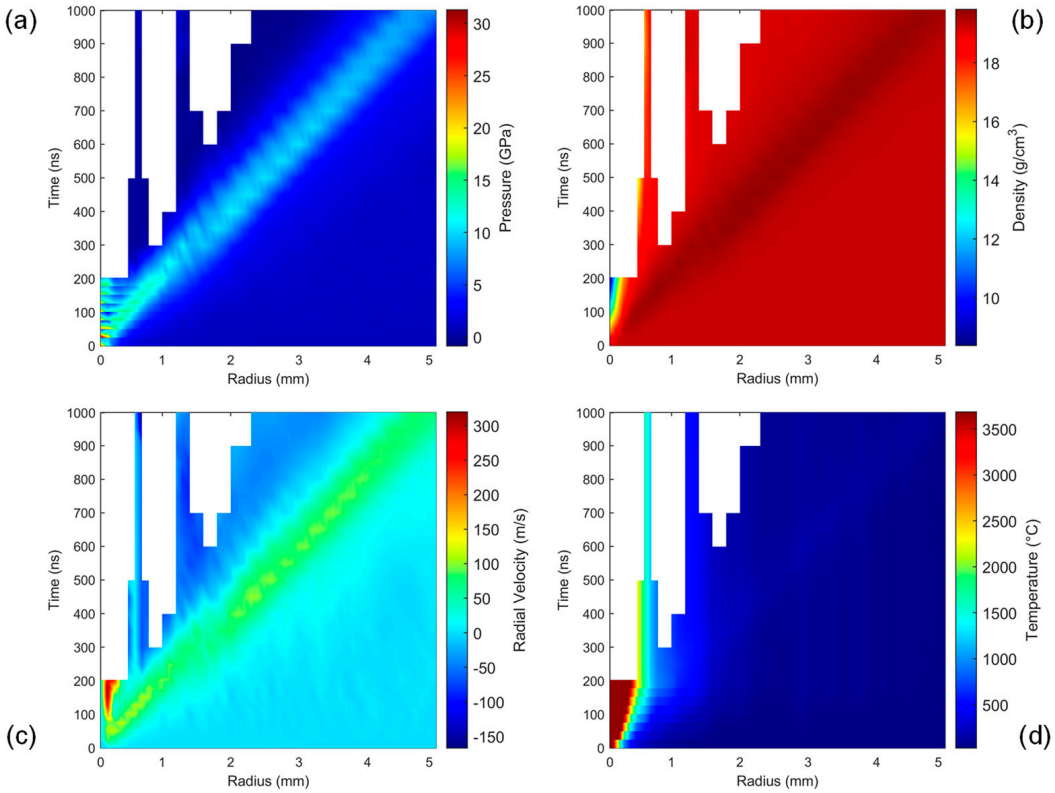

Figure 9. Pressure (**a**), density (**b**), particle velocity in radial direction (**c**), and temperature (**d**) distributions by varying the radius at the impacted base (L_0 of Figure 5).

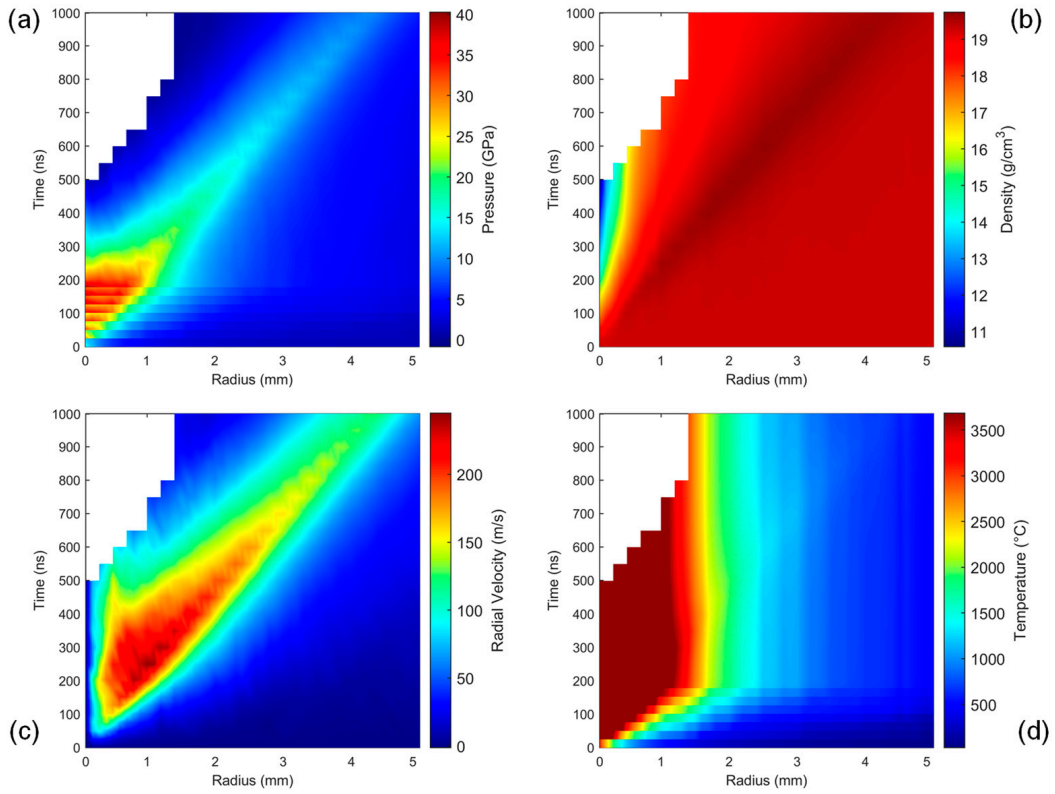

Figure 10. Pressure (**a**), density (**b**), particle velocity in radial direction (**c**), and temperature (**d**) distributions by varying the radius at 50 cm from the impacted base (L_{50} of Figure 5).

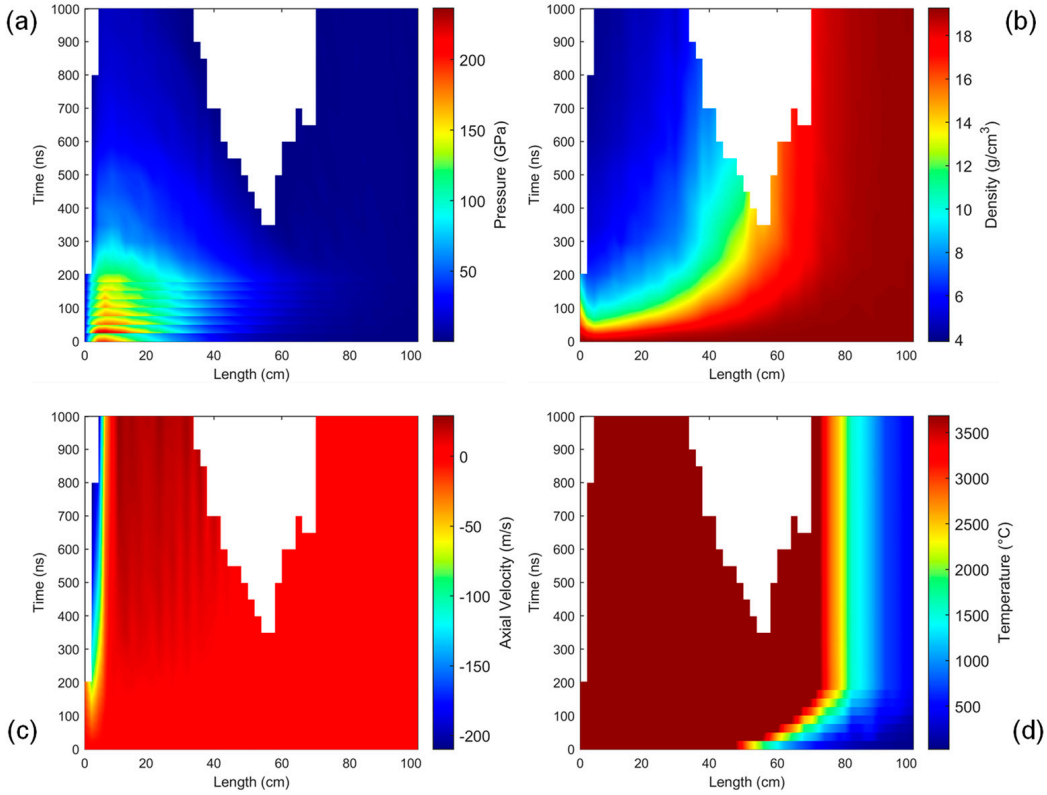

Figure 11. Pressure (**a**), density (**b**), particle velocity in axial direction (**c**), and temperature (**d**) distributions as a function of the length at R = 0 mm (axis of symmetry) (R_0 of Figure 5).

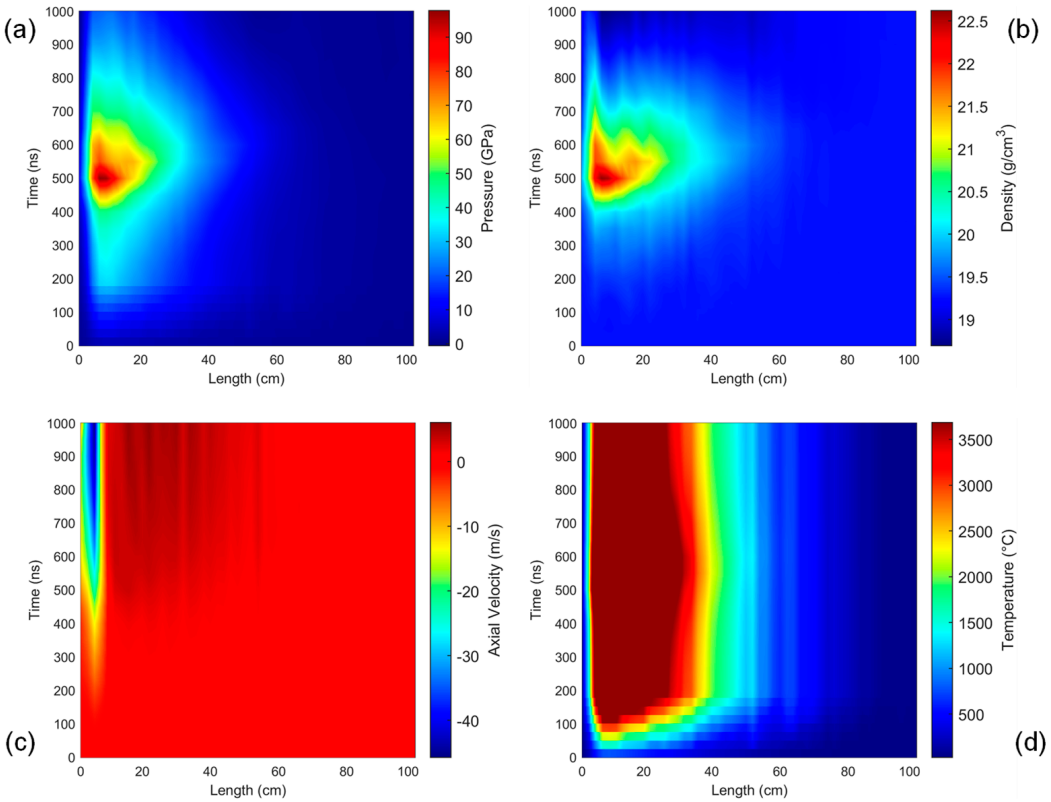

Figure 12. Pressure (**a**), density (**b**), particle velocity in axial direction (**c**), and temperature (**d**) distributions at the radial position of 2.5 mm ($R_{2.5}$ of Figure 5).

Figures 9 and 10 shows the distributions of the same quantities on the impacted base of the component and for a depth of 50 cm from the impacted base, respectively. The previously made considerations are still valid even if some specific comments must be stated. First of all, lower values of pressure, temperature, and particle velocity were reached combined with a less severe reduction of the density in the inner part and a limitation of the molten portion. This because as observable in Figures 1 and 7, the map of the deposited energy was not cylindrical. Considering the base, indicated with L_0 (see Figure 9), some elements failed because the minimum pressure became lower than P_{spall}. The nonsolid portion was limited, and the shockwave travel occurred entirely in solid material. Considering the depth of 50 cm from the impacted base, indicated with L_{50} (see Figure 10), the molten region extended up to a radius of 1.5 mm, and starting from 400 ns, the shock propagation was in the solid part.

In LS-DYNA, the energy balance is performed by the routine of the EOS; at each time step, the total internal energy of each element is calculated by adding the increment with respect to the calculation performed at the previous time step. The increment is the sum of two main contributions: the mechanical work, due to deformation, and the external work. In turn, the mechanical work is composed of deviatoric and hydrodynamic components. In case of pure structural analysis, once the total internal energy is calculated, the temperature update is performed by the routine of the flow stress material model (J–C in this case). Under the assumption of the adiabatic process, the internal energy is converted in temperature considering the density and the specific heat capacity for the solid state at room temperature as the proportional factors. This implies that the temperature calculation does not take the modification of the specific heat capacity and that of the melting temperature, which are information derivable from the EOS, into account. The temperature evaluation, as reported in Figures 8–12, was strictly correct only in the solid part. Nevertheless, the temperature distribution was used to obtain a rough estimation of which part of the component was solid or not.

The next step was the analysis of the results fixing the radius and observing the time evolution as a function of the longitudinal coordinate; this was performed to evaluate the axial wave. The behavior of the axis of the component (R_0) is reported in Figure 11. During the simulated time, nothing apparently moved in the axial direction: pressure, density, and temperature changed during the deposition phase and during the subsequent rarefaction phase but no waves in axial direction were appreciable. The maximum pressure was reached after the arrival of the second bunch and was almost kept until the end of the deposition. After the end of the deposition, the pressure reduced for the expansion consequent to the radial wave propagation. The failure criteria were satisfied for elements behind and above the portion in which the deposited energy was high. The molten area extended along the component up to 80 cm from the impacted base. The axial velocity was high (in absolute value) only near the base because the material expanded toward the external being a free surface. Figure 12 shows the results obtained at a radial coordinate of 2.5 mm, which is quite far from the beam axis to be characterized by low values of the deposited energy (see Figure 7). This implies that the deposition phase was responsible for a modest increment in pressure, while the pressure grew significantly when the shock front arrived.

In Figure 13, the maps of the von Mises stress are reported. As it is possible to notice, it was zero where the temperature exceeded the melting value. In the portion of the component where the temperature was high, the von Mises stress was low, and a pure hydrodynamic approach could be sufficient because the mechanical strength was negligible. Conversely, the material strength and the deviatoric stresses were of importance (or even the dominant part of the stress) in the portion of material where less energy was deposited: the internal higher pressure status generated circumferential stresses able to induce high deviatoric stresses.

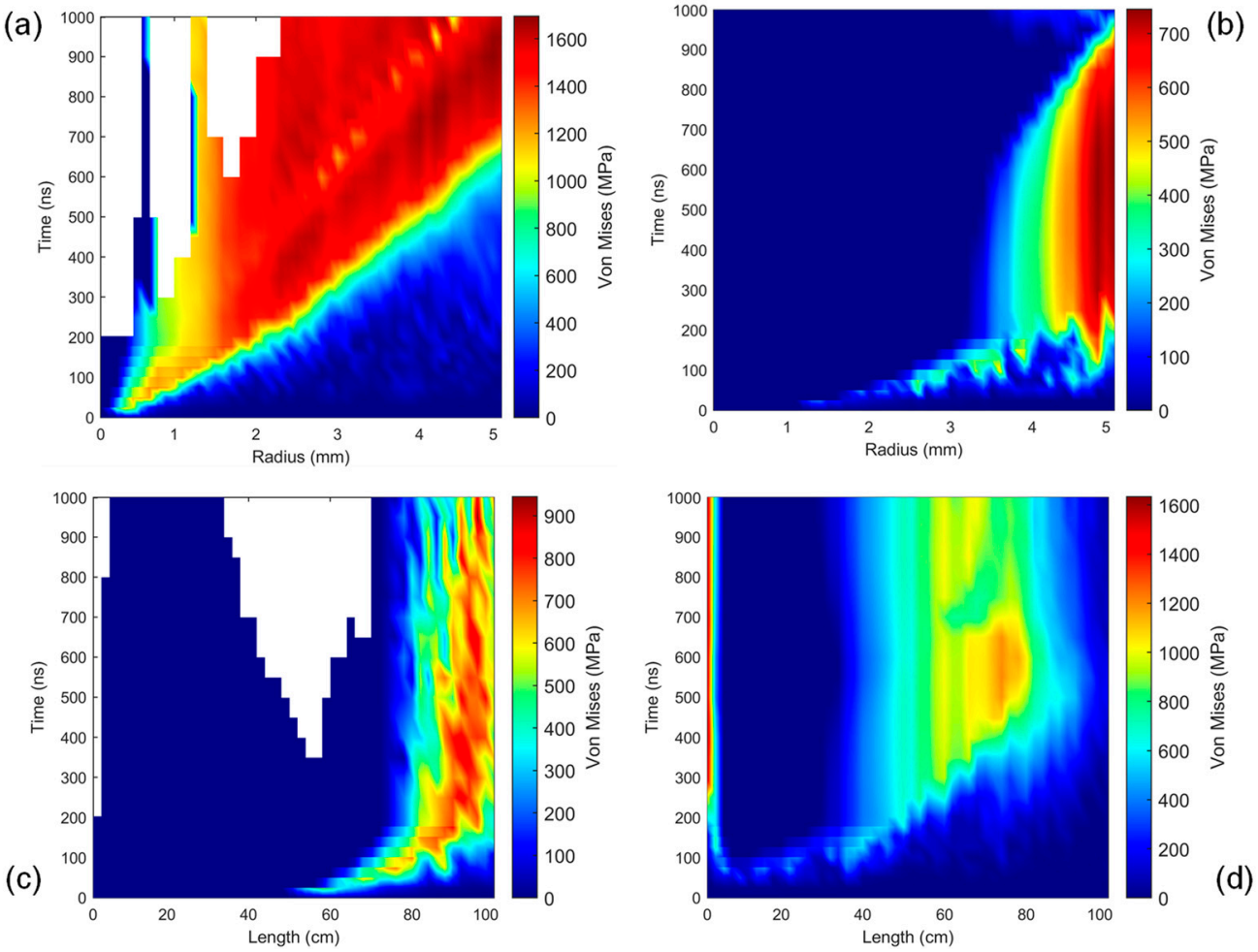

Figure 13. Von Mises stress distributions at (**a**) L_0, (**b**) L_{Emax}, (**c**) R_0, and (**d**) $R_{2.5}$ (see Figure 5).

Another possible visualization of the results is the observation of the paths followed by the elements on the EOS surface. In Figure 14, the EOS is reported in the pressure–energy plane varying the density: the grey lines plotted as background are the isodensity curves of the tabular SESAME EOS for Tungsten. The paths followed by three elements are reported. Figure 14a shows the path of the element in which the maximum energy was deposited (P_1). As a consequence of the energy deposition of the first bunch, it experienced a sudden increase in its internal energy, which passed from 0 to E_1. This jump was made with a negligible variation in the material density (isochoric transformation) and was associated with the pressure increase. During the 25 ns of void before the arrival of the next bunch, this element expanded reaching lower values of pressure, density, and energy (isentropic release), in accordance with the possible states predicted by the EOS. The state in which the expansion ended represented the initial condition for the second bunch and so on. When no more bunches hit the component, the free expansion started. Figure 14b shows the path of two elements: P_2 is located at a radius of 2.5 mm at the same axial coordinate of the element in which there is the maximum deposition and P_3 is located at a radius of 2.5 mm at the axial coordinate of 50 cm from the impacted base. Both of them are located in a part of the component in which the deposited energy was relatively low. In these elements, the deposition phase was responsible for a continuous and moderate increment in pressure without a significant modification in density. Conversely, the state of these elements considerably changed because of the crossing of the shock front: pressure, density, and energy increased (during the shocking phase) and then decreased (during the releasing phase). What happen to each element during the free expansion phases depended on the global redistribution of the stress on the component: as illustrated by

these examples, an element could expand (reaching lower value of pressure and density), or compress (reaching higher value of pressure and density), with the aim of reaching the global equilibrium condition.

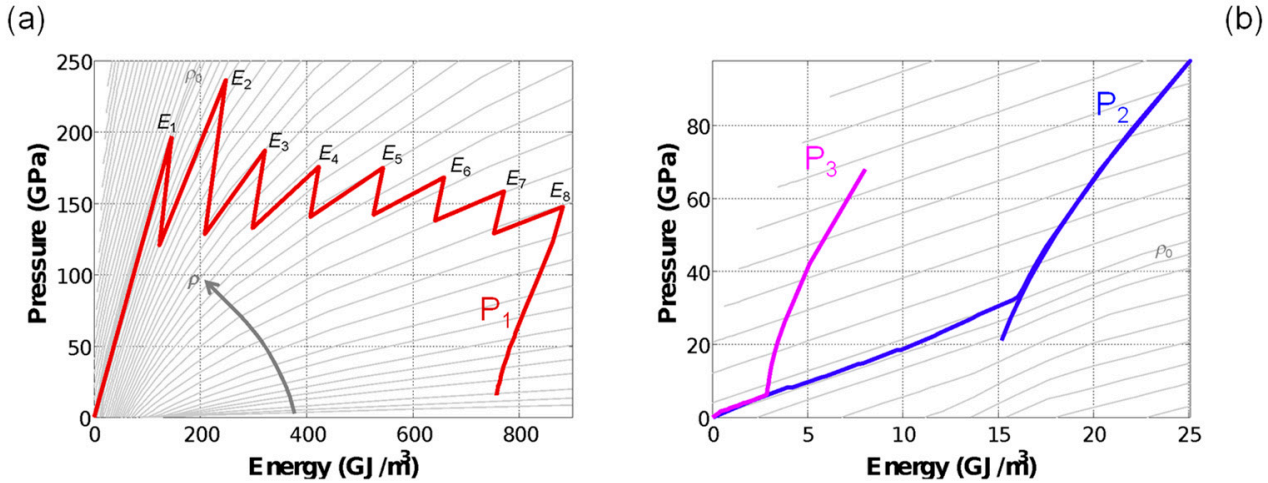

Figure 14. Equation of state of tungsten visualized in the pressure versus energy plane varying the density. The diagrams represent the *P-E-ρ* evolution of three elements: P_1 is situated where there was the maximum of the energy deposition (**a**); P_2 and P_3 are situated far from this region (**b**).

6. Conclusions

In the present paper, the analysis of the effects induced in solid structures by the propagation of shockwave generated from the impact between the material and high-energy particle beam was discussed. First of all, the comparison between planar and cylindrical shockwave was generally discussed, which allowed to focus on the specific characteristics of the axisymmetric waves. In this case, the propagating wave reduces its amplitude moving toward increasing radii and produces a strong rarefaction (hydrostatic tensile state of stress) beyond the shock front.

The second part of the paper was related to the research activities on materials and structures for the LHC at CERN. The prediction of the mechanical response and the induced damage is important for some critical components (such as the beam intercepting devices) installed on the machine. When a high-energy particle beam interacts with a solid structure, it deposits its energy inside the hit material. The deposition induces a sudden nonuniform increase in temperature, energy, and pressure and provokes the generation of axisymmetric wave. Depending on the energy level, the impact condition and the time duration of the phenomena, several scenarios can develop.

In the present study, the impact against a cylindrical tungsten bar hit at the center of one basis by eight proton bunches at 7 TeV of the LHC was simulated. The geometry considered was a cylinder 1 m long and with a radius of 10 mm. The evaluation of the energy deposited on the impacted material was performed by the FLUKA Team at CERN, using the statistical code, called FLUKA. The output of the calculation was the energy map on the component which was used as input data for the FE calculations. They were performed in LS-DYNA in the case of Lagrangian and pure structural analysis and solved with an explicit time integration method. The fact that both the target geometry and the load applied, in terms of energy deposition, are axisymmetric allowed to reduce the 3D problem to a 2D one, so the component was modeled with 2D axisymmetric elements. The material behavior was described by a multiphase EOS combined with both strength and failure models. The results were analyzed in terms of temporal evolution of pressure, density, temperature, particle velocity, and von Mises stress. The typical approach used in case of 1D wave propagation was followed to investigate both radial and axial waves. Analysis of the evolution of these quantities was conducted by varying a single spatial coordinate at a time. The results showed that the high amount of energy delivered on the

impacted (central) part of the component acted as an explosive inducing the shockwave generation and its travel from the central zone to the external radii. The pressure evolution was strictly related to the density changes and the energy deposition, in accordance with the EOS. The traveling shockwave produced a strong rarefaction in the material placed behind because of the release wave and a compression in the material placed ahead of it with the possibility to strongly change its state. Fixing the attention on a single element, the evolution of the states on the EOS surface was performed. Finally, a rough estimation of the induced damage was also performed.

Author Contributions: Conceptualization, M.S. and L.P.; methodology, M.S. and L.P.; investigation, M.S. and L.P.; data curation, M.S. and L.P.; writing—original draft preparation, M.S. and L.P.; writing—review and editing, M.S. and L.P. All authors have read and agreed to the published version of the manuscript.

Funding: This research received no external funding.

Institutional Review Board Statement: Not applicable.

Informed Consent Statement: Not applicable.

Data Availability Statement: The raw/processed data required to reproduce these findings cannot be shared at this time as the data also forms part of an ongoing study.

Acknowledgments: This project has received funding from the European Union's Horizon 2020 Research and Innovation programme under grant agreement no 730871. The author thanks the EN-MME group of CERN for providing data, geometry, and loading condition and the EN-STI group of CERN for FLUKA calculation on hit components.

Conflicts of Interest: The authors declare no conflict of interest.

References

1. Brüning, P.; Collier, P.; Lebrun, S.; Myers, R.; Ostojic, J.; Poole, E.; Proudlock, P. *LHC Design Report*; CERN Yellow Reports: Monographs; CERN: Geneva, Switzerland, 2004.
2. Apollinari, G.; Alonso, I.B.; Bruning, O.; Fessia, P.; Lamont, M.; Rossi, E.L.; Tavian, L. *High-Luminosity Large Hadron Collider (HL-LHC) Technical Design Report v.0.1*; CERN Yellow Reports: Monographs 4; CERN: Geneva, Switzerland, 2017.
3. Assmann, R.; Bailey, R.; Brüning, O.; Sanchez, O.D.; de Rijk, G.; Jimenez, J.M.; Myers, S.; Rossi, L.; Tavian, L.; Todesco, E.; et al. *First Thoughts on a Higher-Energy LHC*; CERN-ATS-2010-177; CERN: Geneva, Switzerland, 2010.
4. Abada, A.; the FCC Collaboration; Abbrescia, M.; AbdusSalam, S.S.; Abdyukhanov, I.; Fernandez, J.A.; Abramov, A.; Aburaia, M.; Acar, A.O.; Adzic, P.R.; et al. FCC-hh: The Hadron Collider. *Eur. Phys. J. Spec. Top.* **2019**, *228*, 755–1107. [CrossRef]
5. Beringer, J.; Arguin, J.F.; Barnett, R.M.; Copic, K.; Dahl, O.; Groom, D.E.; Lin, C.J.; Lys, J.; Murayama, H.; Wohl, C.G.; et al. Review of Particle Physics. *Phys. Rev. D* **2012**, *86*, 10001. [CrossRef]
6. Mokhov, N.V. Beam–Materials Interactions. *Rev. Accel. Sci. Technol.* **2013**, *6*, 275–290. [CrossRef]
7. Kalinovskii, A.N.; Mokhov, N.V.; Nikitin, Y.P. *Passage of High-Energy Particles through Matter*; American Institute of Physics: New York, NY, USA, 1989.
8. Ferrari, A.; Ranft, J.; Sala, P.R.; Fassò, A. *FLUKA: A Multi-Particle Transport Code*; CERN-2005-010; CERN Yellow Reports: Monographs, 2005. [CrossRef]
9. Battistoni, G.; Cerutti, F.; Fasso, A.; Ferrari, A.; Muraro, S.; Ranft, J.; Roesle, S.; Sala, P.R. *The FLUKA Code: Description and Benchmarking, Hadronic Shower Simulation Workshop*; Albrow, M., Raja, R., Eds.; American Institute of Physics: New York, NY, USA, 2007.
10. Agostinelli, S.; Allison, J.; Amako, K.; Apostolakis, J.; Araujo, H.; Arce, P.; Asai, M.; Axen, D.; Banerjee, S.; Barrand, G.; et al. Geant4—A simulation toolkit. *Nucl. Instrum. Methods Phys. Res. Sect. A Accel. Spectrom. Detect. Assoc. Equip.* **2003**, *506*, 250–303. [CrossRef]
11. Allison, J.; Amako, K.; Apostolakis, J.; Araujo, H.; Dubois, P.A.; Asai, M.; Barrand, G.; Capra, R.; Chauvie, S.; Chytracek, R.; et al. Geant4 developments and applications. *IEEE Trans. Nucl. Sci.* **2006**, *53*, 270–278. [CrossRef]
12. Mokhov, N.V.; James, C.C. *The MARS Code System User's Guide Version 15(2016)*; Fermi National Accelerator Lab.: Batavia, IL, USA, 2017. [CrossRef]
13. Goorley, T.; James, M.; Booth, T.; Brown, F.; Bull, J.; Cox, L.J.; Durkee, J.; Elson, J.; Fensin, M.; Forster, R.A.; et al. Initial MCNP6 Release Overview. *Nucl. Technol.* **2012**, *180*, 298–315. [CrossRef]
14. Niita, K.; Sato, T.; Iwase, H.; Nose, H.; Nakashima, H.; Sihver, L. PHITS—A particle and heavy ion transport code system. *Radiat. Meas.* **2006**, *41*, 1080–1090. [CrossRef]

15. Fortov, V.E.; Goel, B.; Munz, C.-D.; Ni, A.L.; Shutov, A.; Vorbiev, Y.O.; Fortov, V.E.; Goel, B.; Munz, C.D.; Ni, A.L.; et al. Numerical simulations of nonstationary fronts and interfaces by the Godunov method in moving grids. *Nucl. Sci. Eng.* **1996**, *123*, 169. [CrossRef]
16. *ANSYS AUTODYN User Manual*; Release 15.0; SAS IP, Inc.: Canonsburg, PA, USA, 2013.
17. Gladman, B. *Keyword User's Manual—Volume I—Version 971*; LSTC (Livermore Software Technology Corporation): Livermore, CA, USA, 2007; ISBN 0-9778540-2-7.
18. Tahir, N.A.; Goddard, B.; Kain, V.; Schmidt, R.; Shutov, A.; Lomonosov, I.V.; Piriz, A.R.; Temporal, M.; Hoffmann, D.H.H.; Fortov, V.E. Impact of 7-TeV/c Large Hadron Collider proton beam on a copper target. *J. Appl. Phys.* **2005**, *97*, 83532. [CrossRef]
19. Ryazanov, A.I.; Klaptsov, A.V.; Pavlov, S.A.; Assmann, R.; Ferrari, A.; Schmidt, R. Shock wave propagation near 7 TeV proton beam in LHC collimator materials. In Proceedings of the Workshop on High Intensity High Brightness Hadron Beams 2006 (HB2006), Tsukuba, Japan, 29 May–2 June 2006.
20. Tahir, N.A.; Schmidt, R.; Brugger, M.; Assmann, R.; Shutov, A.; Lomonosov, I.V.; Gryaznov, V.; Piriz, A.R.; Udrea, S.; Hoffmann, D.H.H.; et al. Generation of warm dense matter and strongly coupled plasmas using the High Radiation on Materials facility at the CERN Super Proton Synchrotron. *Phys. Plasmas* **2009**, *16*, 82703. [CrossRef]
21. Tahir, N.; Schmidt, R.; Brügger, M.; Assmann, R.; Shutov, A.; Lomonosov, I.; Fortov, V.; Piriz, A.R.; Deutsch, C.; Hoffmann, D. Interaction of Super Proton Synchrotron beam with solid copper target: Simulations of future experiments at HiRadMat facility at CERN. *Nucl. Instruments Methods Phys. Res. Sect. A: Accel. Spectrometers, Detect. Assoc. Equip.* **2009**, *606*, 186–192. [CrossRef]
22. Tahir, N.; Schmidt, R.; Shutov, A.; Lomonosov, I.; Gryaznov, V.; Piriz, A.; Deutsch, C.; Fortov, V. The Large Hadron Collider and the Super Proton Synchrotron at CERN as tools to Generate Warm Dense Matter and Non-Ideal Plasmas. *Contrib. Plasma Phys.* **2011**, *51*, 299–308. [CrossRef]
23. Dallocchio, A. Study of Thermo-Mechanical Effects Induced in Solids by High Energy Particle Beams: Analytical and Numerical Methods. Ph.D. Thesis, Politecnico di Torino, Torino, Italy, 2008.
24. Pasquali, M.; Bertarelli, A.; Accettura, C.; Berthome, E.; Bianchi, L.; Bolz, P.; Carra, F.; Fichera, C.; Frankl, M.I.; Furness, T.; et al. Dynamic Response of Advanced Materials Impacted by Particle Beams: The MultiMat Experiment. *J. Dyn. Behav. Mater.* **2019**, *5*, 266–295. [CrossRef]
25. Cauchi, M.; Assmann, R.W.; Bertarelli, A.; Carra, F.; Cerutti, F.; Lari, L.; Redaelli, S.; Mollicone, P.; Sammut, N. Thermomechanical response of Large Hadron Collider collimators to proton and ion beam impacts. *Phys. Rev. Spéc. Top.-Accel. Beams* **2015**, *18*, 41002. [CrossRef]
26. Martin, C.T.; Perillo-Marcone, A.; Calviani, M.; Muñoz-Cobo, J.-L. CERN antiproton target: Hydrocode analysis of its core material dynamic response under proton beam impact. *Phys. Rev. Accel. Beams* **2016**, *19*, 73402. [CrossRef]
27. Martin, C.T.; Solieri, N.; Fornasiere, E.; Descarrega, J.B.; Calviani, M.; Espadanal, J.C.; Perillo-Marcone, A.; Spätig, P. First observation of spalling in tantalum at high temperatures induced by high energy proton beam impacts. *Eur. J. Mech.-A/Solids* **2020**, *85*, 104149. [CrossRef]
28. Scapin, M.; Peroni, L.; Dallocchio, A. Damage evaluation in metal structures subjected to high energy deposition due to particle beams. *J. Phys. Conf. Ser.* **2011**, *305*, 12062. [CrossRef]
29. Scapin, M.; Peroni, L.; Dallocchio, A.; Bertarelli, A. Shock Loads Induced on Metal Structures by LHC Proton Beams: Modelling of Thermo-Mechanical Effects. *Appl. Mech. Mater.* **2011**, *82*, 338–343. [CrossRef]
30. Scapin, M.; Peroni, L.; Bertarelli, A.; Dallocchio, A. Numerical simulations of tungsten targets HIT by LHC proton beam. In Proceedings of the 4th International Conference on Computational Methods for Coupled Problems in Science and Engineering COUPLED PROBLEMS 2011, Kos, Greece, 20–22 June 2011; pp. 413–423.
31. Bertarelli, A.; Boccone, V.; Carra, F.; Cerutti, F.; Dallocchio, A.; Mariani, N.; Peroni, L.; Scapin, M. Limits for beam induced damage: Reckless or too cautious? In Proceedings of the Chamonix 2011 workshop on LHC performance, Chamonix, France, 24–28 January 2011.
32. Quaranta, E.; Bertarelli, A.; Bruce, R.; Carra, F.; Cerutti, F.; Lechner, A.; Redaelli, S.; Skordis, E.; Gradassi, P. Modeling of beam-induced damage of the LHC tertiary collimators. *Phys. Rev. Accel. Beams* **2017**, *20*, 091002. [CrossRef]
33. Scapin, M.; Peroni, L.; Boccone, V.; Cerutti, F. Effects of high-energy intense multi-bunches proton beam on materials. *Comput. Struct.* **2014**, *141*, 74–83. [CrossRef]
34. Tahir, N.A.; Sancho, J.B.; Shutov, A.; Schmidt, R.; Piriz, A.R. Impact of high energy high intensity proton beams on targets: Case studies for Super Proton Synchrotron and Large Hadron Collider. *Phys. Rev. Spéc. Top.-Accel. Beams* **2012**, *15*. [CrossRef]
35. Nie, Y.; Fichera, C.; Mettler, L.; Carra, F.; Schmidt, R.; Tahir, N.A.; Bertarelli, A.; Wollmann, D. Simulation of hydrodynamic tunneling induced by high-energy proton beam in copper by coupling computer codes. *Phys. Rev. Accel. Beams* **2019**, *22*, 014501. [CrossRef]
36. Tahir, N.A.; Burkart, F.; Schmidt, R.; Shutov, A.; Wollmann, D.; Piriz, A.R. Beam Induced Hydrodynamic Tunneling in the Future Circular Collider Components. *Phys. Rev. Accel. Beams* **2016**, *19*, 081002. [CrossRef]
37. Tahir, N.A.; Burkart, F.; Shutov, A.; Schmidt, R.; Wollmann, D.; Piriz, A.R. Simulations of beam-matter interaction experiments at the CERN HiRadMat facility and prospects of high-energy-density physics research. *Phys. Rev. E* **2014**, *90*, 063112. [CrossRef] [PubMed]
38. Tahir, N.; Burkart, F.; Schmidt, R.; Shutov, A.; Wollmann, D.; Piriz, A. High energy density physics effects predicted in simulations of the CERN HiRadMat beam–target interaction experiments. *High Energy Density Phys.* **2016**, *21*, 27–34. [CrossRef]

39. Bertarelli, A.; Bruce, R.; Carra, F.; Dallocchio, A.; Guinchard, M.; Mariani, N.; Lari, L.; Redaelli, S.; Rossi, A. Updated robustness limits for collimator materials. In Proceedings of the MPP Workshop, Annecy, France, 11–13 March 2013; Volume 108–112.
40. Efthymiopoulos, I. HiRadMat: A new irradiation facility for material testing at CERN. In Proceedings of the Second IPAC 2011, San Sebastian, Spain, 4–9 September 2011; pp. 1665–1667.
41. Bertarelli, A.; Berthome, E.; Boccone, V.; Carra, F.; Cerutti, F.; Charitonidis, N.; Charrondiere, C.; Dallocchio, A.; Fernandez, P.; Carmona; et al. An experiment to test advanced materials impacted by intense protonpulses at CERN HiRadMat facility. *Nucl. Instrum. Methods Phys. Res. B* **2013**, *308*, 88–99. [CrossRef]
42. Carra, F.; Bertarelli, A.; Berthomé, E.; Fichera, C.; Furness, T.; Guinchard, M.; Mettler, L.K.; Portelli, M.; Redaelli, S.; De Frutos, O.S. The "Multimat" experiment at CERN HiRadMat facility: Advanced testing of novel materials and instrumentation for HL-LHC collimators. *J. Phys. Conf. Ser.* **2017**, *874*, 012001. [CrossRef]
43. AMartin, T.; Perillo-Marcone, A.; Calviani, M.; Gentini, L.; Butcher, M.; Muñoz-Cobo, J.L. Experiment exposing refractory metals to impacts of 440 GeV/c proton beams for the future design of the CERN antiproton production target: Experiment design and online results. *Phys. Rev. Accel. Beams* **2019**, *22*, 13401. [CrossRef]
44. Bertarelli, A.; Dallocchio, A.; Garlasche, M.; Gentini, L.; Gradassi, P.; Guinchard, M.; Redaelli, S.; Rossi, A.; Sacristan De Frutos, O.; Carra, F.; et al. Novel materials for collimators at LHC and its upgrades. In Proceedings of the HB2014, East Lansing, MI, USA, 10–14 November 2014; pp. 438–442, ISBN 978-3-95450-173-1.
45. Martin, C.T.; Calviani, M.; Perillo-Marcone, A.; Ferriere, R.; Solieri, N.; Butcher, M.; Grec, L.-M.; Espadanal, J.C. Scaled prototype of a tantalum target embedded in expanded graphite for antiproton production: Design, manufacturing, and testing under proton beam impacts. *Phys. Rev. Accel. Beams* **2018**, *21*, 073001. [CrossRef]
46. Torregrosa, C.; Calviani, M.; Solieri, N.; Canhoto, J.; Perillo-Marcone, A.; Ferriere, R.; Fornasiere, E.; Busom, J.; Dickinson, B. First prototypes of the new design of the CERN's antiproton production targetMater. *Des. Process. Commun.* **2019**, *1*, e38. [CrossRef]
47. Carra, F.; Charrondiere, C.; Guinchard, M.; de Frutos, O.S. Design and Construction of an Instrumentation System to Capture the Response of Advanced Materials Impacted by Intense Proton Pulses. *Shock Vib.* **2021**, *2021*, 1–20. [CrossRef]
48. Gobbi, G.; Bertarelli, A.; Carra, F.; Guardia-Valenzuela, J.; Redaelli, S. Novel LHC collimator materials: High-energy Hadron beam impact tests and nondestructive postirradiation examination. *Mech. Adv. Mater. Struct.* **2019**, *27*, 1518–1530. [CrossRef]
49. Portelli, M.; Pasquali, M.; Carra, F.; Bertarelli, A.; Mollicone, P.; Sammut, N.; de Frutos, Ó.S.; Valenzuela, J.G.; Neubauer, E.; Kitzmantel, M.; et al. Thermomechanical Characterisation of Copper Diamond and Benchmarking with the MultiMat Experiment. *Shock Vib.* **2021**, *2021*, 1–18. [CrossRef]
50. Meyers, M.A. *Dynamic Behaviour of Materials*; J. Wiley & Sons: Hoboken, NY, USA, 1994; ISBN 047158262.
51. Zukas, A.J. *High Velocity Impact Dynamics*; J. Wiley & Sons: New York, NY, USA, 1990; ISBN 0471514446.
52. Zukas, A.J. *Introduction to Hydrocodes*; Elsevier Science & Technology: Amsterdam, The Netherlands, 2004; ISBN 0080443486.
53. Morena, A.; Peroni, L. Numerical Simulations of Laser-Induced Shock Experiments on Graphite. *Materials* **2021**, *14*, 7079. [CrossRef]
54. Davis, I.L. *Wave Propagation in Solids and Fluids*; Springer: New York, NY, USA, 1998; ISBN I3 978-1-4612-8390-4. [CrossRef]
55. Scapin, M.; Peroni, L.; Dallocchio, A. Effects induced by LHC high energy beam in copper structures. *J. Nucl. Mater.* **2012**, *420*, 463–472. [CrossRef]
56. Scapin, M.; Peroni, L.; Dallocchio, A. Thermo-Mechanical Modelling of High Energy Particle Beam Impacts. In *Numerical Modeling of Materials under Extreme Conditions*; Springer: Berlin, Heidelberg, 2014; pp. 87–106. [CrossRef]
57. Johnson, G.R.; Cook, W.H. A Constitutive Model and Data for Metals Subjected to Large Strains, High Strain Rates, and High Temperatures. In Proceedings of the 7th International Symposium on Ballistics, The Hague, The Netherlands, 19–21 April 1983; pp. 541–547.
58. Tarabay, A.; Seaman, L.; Curran, D.R.; Kanel, G.I.; Razorenov, S.V.; Utkin, A.V. *Spall Fracture*; Springer: New York, NY, USA, 2003; ISBN 0-387-95500-3.
59. Lennon, A.; Ramesh, K. The thermoviscoplastic response of polycrystalline tungsten in compression. *Mater. Sci. Eng. A* **2000**, *276*, 9–21. [CrossRef]
60. Kerley, G.I. *Equations of State for Be, Ni, W, and AU*; SANDIA REPORT SAND 2003-3784; Sandia National Laboratories: Albuquerque, NM, USA, 2003.